Progress In Electromagnetics Research, Vol. 146, 155–165, 2014

Efficient Analysis of Electromagnetic Fields for Designing Nanoscale Antennas by Using a Boundary Integral Equation Method with Fast Inverse Laplace Transform

Seiya Kishimoto, Tatsuichiro Okada, Shinichiro Ohnuki*, Yoshito Ashizawa, and Katsuji Nakagawa

Abstract—In this paper, we investigate electromagnetic problems for nanoscale antennas by using a boundary integral equation method with fast inverse Laplace transform. The antennas are designed for realizing ultra-fast and high-density magnetic recording. Characteristics of nanoscale antennas are discussed in terms of eigenmodes and time domain responses of electric fields. Our computational method is highly efficient and the computational cost can be reduced by selecting coarse time-step size and performing parallel computation.

1. INTRODUCTION

As can be seen from recent developments in nanotechnology, analysis of electromagnetic phenomena for nanoscale objects plays an important role [1, 2]. In this paper, electromagnetic problems for nanoscale antennas are investigated by a boundary integral equation method with fast inverse Laplace transform (BIEM-FILT) [3, 4]; novel antennas are designed to realize ultra-fast and high-density magnetic recording using localized circularly polarized light [5–8]. For this state-of-the-art technology, high intensity and localized circularly polarized light is required near the antenna. Here, the size of the antenna is much smaller than the incident wavelength and the generated light is enhanced by plasmon resonances which can be considered as electrostatic phenomena [9–11]. Characteristics of the antenna are evaluated in terms of eigenmodes and time domain responses of electromagnetic fields. The former are required to generate localized high intensity light and the latter are important for estimating the magnetic recording process due to variation of the electric field intensity and stability of the localized light.

BIEM-FILT can remove computational restriction on selecting time-step size and is suitable for parallel computing. We verify that the computational error of the time domain response can be controlled in spite of time-step size. Acceleration of BIEM-FILT is achieved by performing parallel computation, and load distribution techniques are also discussed.

2. FORMULATION

Figure 1 shows a nanoscale object and coordinate systems. We assume that the object is a homogeneous dispersible dielectric which is expressed by the Lorentz-Drude model [12] as

$$\varepsilon(s) = \varepsilon_0 \left[1 + \frac{A_0 \omega_p^2}{s^2 + \gamma_0 s} + \sum_{j=1}^{K} \frac{A_j \omega_p^2}{s^2 + \gamma_j s + \omega_j^2} \right], \tag{1}$$

Received 17 August 2013, Accepted 16 May 2014, Scheduled 23 May 2014

* Corresponding author: Shinichiro Ohnuki (ohnuki.shinichiro@nihon-u.ac.jp).
The authors are with the College of Science and Technology, Nihon University, 1-8-14 Surugadai, Kanda, Chiyoda-ku, Tokyo 101-8308, Japan.

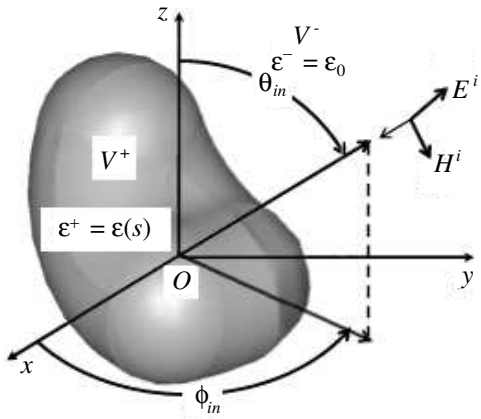

Figure 1. Geometry and coordinate system. The object is arbitrarily shape with homogeneous dispersible dielectric media.

where s is the complex frequency, ω_p the plasma frequency, and K the number of oscillators with the frequency ω_j. γ_0 and γ_j are collision frequencies, and A_0 and A_j are material constants.

When the object permittivity is negative and the free-space wavelength is large in comparison with object dimensions, plasmon resonance can be observed at certain frequencies [4, 9–11]. Since the wavelength is much longer than objects, the resonances can be considered as electrostatic phenomena. They appear at specific negative values of dielectric permittivity for which source-free electrostatic fields may exist.

Considering the quasi-static approximation, the scattered fields can be expanded in terms of the complex frequency s

$$\mathbf{E}^{\pm} = \mathbf{E}_0^{\pm} + (s\sqrt{\varepsilon_0\mu_0}d)\mathbf{E}_1^{\pm} + (s\sqrt{\varepsilon_0\mu_0}d)^2\mathbf{E}_2^{\pm} + \ldots, \tag{2}$$

$$\mathbf{H}^{\pm} = \mathbf{H}_0^{\pm} + (s\sqrt{\varepsilon_0\mu_0}d)\mathbf{H}_1^{\pm} + (s\sqrt{\varepsilon_0\mu_0}d)^2\mathbf{H}_2^{\pm} + \ldots, \tag{3}$$

where, ε_0 and μ_0 are the permittivity and the permeability in free space, respectively.

For zero order terms in Eq. (2), the electric fields satisfy the following boundary condition;

$$\mathbf{n} \cdot \left(\varepsilon(s)\mathbf{E}_0^{+} - \varepsilon_0\mathbf{E}_0^{-}\right) = (\varepsilon_0 - \varepsilon(s))\mathbf{n} \cdot \mathbf{E}_0^{i}\hat{f}(s)_{in}, \tag{4}$$

where, $\hat{f}_{in}(s)$ is the spectrum of the incident pulse, and $\mathbf{n}$ is a unit vector of outward normal to the surface of the object. The normal components of electric fields at the boundary are given by

$$\mathbf{n} \cdot \mathbf{E}^{\pm}(\mathbf{r}) = \mp\frac{\sigma(\mathbf{r})}{2\varepsilon_0} + \frac{1}{4\pi\varepsilon_0}\oint_{\Omega}\sigma(\mathbf{r}')\frac{\mathbf{n} \cdot (\mathbf{r} - \mathbf{r}')}{|\mathbf{r} - \mathbf{r}'|^3}d\Omega', \tag{5}$$

where σ indicates the electric charge density on the surface.

Considering the boundary condition, the normal components of the electric flux density are continuous at the boundary, and we can obtain the following homogeneous boundary integral equation:

$$\sigma(\mathbf{r}) - \frac{1}{2\pi}\left(\frac{\varepsilon(s) - \varepsilon_0}{\varepsilon(s) + \varepsilon_0}\right)\oint_{\Omega}\sigma(\mathbf{r}')\frac{\mathbf{n} \cdot (\mathbf{r} - \mathbf{r}')}{|\mathbf{r} - \mathbf{r}'|^3}d\Omega' = 2\varepsilon_0\left(\frac{\varepsilon(s) - \varepsilon_0}{\varepsilon(s) + \varepsilon_0}\right)\mathbf{n} \cdot \mathbf{E}^{i}f_{in}(s). \tag{6}$$

For solving Eq. (6), the unknown surface charge density is expanded in the basis function g_i, such as

$$\sigma(\mathbf{r}) = \sum_{i=1}^{N} a_i g_i(\mathbf{r}), \tag{7}$$

where a_i is the unknown expansion coefficient, and N is their number. The integral equation is discretized by Eq. (7) as

$$\sum_{n=1}^{N} A_{ji}a_i = F_j, \qquad j = 1, 2, \ldots, N, \tag{8}$$

where

$$F_j = 2\varepsilon_0\hat{\lambda}\oint_\Omega \hat{t}_j(\mathbf{r},s)\mathbf{n}\cdot\mathbf{E}^i\hat{f}(s)d\Omega, \tag{9}$$

$$A_{ji} = \oint_\Omega \hat{t}_j(\mathbf{r},s)\hat{g}_i(\mathbf{r},s)d\Omega - \frac{\hat{\lambda}}{2\pi}\oint_\Omega \hat{t}_j(\mathbf{r},s)\oint_\Omega \hat{g}_i\left(\mathbf{r}',s\right)\frac{\mathbf{n}\cdot(\mathbf{r}-\mathbf{r}')}{|\mathbf{r}-\mathbf{r}'|^3}d\Omega' d\Omega, \tag{10}$$

and $\hat{t}_j$ is the testing function. We choose the basis and testing functions as the pulse functions. Solving the matrix equation in Eq. (8), we can obtain the unknown electric charge density.

For the eigenmode analysis, Eq. (6) is transformed into the eigen equationm and trivial solutions are sought [9–11], that is

$$\sigma_k(\mathbf{r}) = \frac{\lambda_k}{2\pi}\oint_\Omega \sigma_k\left(\mathbf{r}'\right)\frac{\mathbf{n}\cdot(\mathbf{r}-\mathbf{r}')}{|\mathbf{r}-\mathbf{r}'|^3}d\Omega', \tag{11}$$

where

$$\lambda_k = \frac{\varepsilon_k-\varepsilon_0}{\varepsilon_k+\varepsilon_0}, \tag{12}$$

k is the mode number. Eigenvalue λ_k is obtained by solving Eq. (11), and the resonance values of permittivity ε_k is found using Eq. (12).

To express the time variation of the surface charge, the set of eigenfunctions σ_k can be used for the expansion of actual boundary charges $\sigma(\mathbf{r},t)$ which is induced on the surface boundary during the excitation process:

$$\sigma(\mathbf{r},t) = \sum_{k=1}^{\infty} a_k(t)\sigma_k(\mathbf{r}), \tag{13}$$

where $a_k(t)$ is the expansion coefficient. Considering the Laplace transform, $a_k(t)$ is transformed into the complex frequency domain, and Eq. (13) can be rewritten as

$$\sigma(\mathbf{r},s) = \sum_{k=1}^{\infty} a_k(s)\sigma_k(\mathbf{r}), \tag{14}$$

where

$$a_k(s) = \beta h_k(s) f_{in}(s), \tag{15}$$

$$h_k(s) = \frac{\varepsilon(s)-\varepsilon_0}{\varepsilon_k-\varepsilon(s)}, \tag{16}$$

and β is determined by the direction of the incident wave and the dipole moments [9]. Surface charge densities $\sigma(\mathbf{r},s)$ are transformed into the time domain by using FILT.

For the transient analysis, the function in the complex frequency domain $F(s)$ is transformed into the time domain by the inverse Laplace transform defined by the Bromwich integral

$$f(t) = \frac{1}{2\pi i}\int_{\gamma-i\infty}^{\gamma+i\infty} F(s)e^{st}ds, \tag{17}$$

where s is a complex frequency. In FILT, the exponential function in the Bromwich integral is approximated by [4, 13]

$$E_{ap}(st,\alpha) = \frac{e^\alpha}{2\cosh(\alpha-st)} = e^{st} - e^{-2\alpha}e^{3st} + e^{-4\alpha}e^{5st} - \ldots = \frac{e^\alpha}{2}\sum_{n=-\infty}^{\infty}\frac{i(-1)^n}{st-\alpha+i(n-0.5)\pi}, \tag{18}$$

where α is the approximate parameter. Using Eq. (18), the inverse Laplace transform can be rewritten as

$$f_{ap}(t) = \frac{1}{2\pi i}\int_{\gamma-i\infty}^{\gamma+i\infty} F(s)E_{ap}(st,\alpha)ds = \frac{e^\alpha}{t}\sum_{n=1}^{\infty}F_n, \tag{19}$$

where

$$F_n = (-1)^n \mathrm{Im}\left[F\left\{\frac{\alpha + i(n-0.5)\pi}{t}\right\}\right]. \tag{20}$$

For the numerical computation, the infinite series in Eq. (19) is truncated as

$$f_{ap}(t) \approx \frac{e^{\alpha}}{t}\sum_{n=1}^{K} F_n, \tag{21}$$

where K is the truncation number of FILT. Here, the series in Eq. (21) is the alternative. Therefore, we can achieve rapid convergence by applying the Euler transformation [13]. Correspondingly, Eq. (21) can be expressed as

$$f_{ap}(t) = \frac{e^{\alpha}}{t}\left(\sum_{n=1}^{K} F_n + 2^{-(p+1)}\sum_{q=1}^{p} A_{pq}F_{K+q}\right), \tag{22}$$

where

$$A_{pp} = 1, \quad A_{pq-1} = A_{pq} + \frac{(p+1)!}{q!(p+1-q)!}, \tag{23}$$

and p is the term number of the Euler transformation.

The computational error of FILT can be easily estimated by Eq. (18) and represented by

$$f(t) - f_{ap}(t) = e^{-2\alpha}f(3t) - e^{-4\alpha}f(5t) + \ldots. \tag{24}$$

When the approximate parameter is large, the error decreases exponentially. The first term is the dominant term for the computational error which can be estimated by $10^{-\alpha}$.

Figure 2 shows the flowchart of BIEM-FILT. To obtain the time domain function, we need to calculate the finite series in Eq. (22) at each time-step. The unknown functions in the complex frequency domain are obtained by BIEM and the computation is not expensive, since the complex frequency s is selected as the limited number of poles for the approximated exponential function. Eq. (22) can be calculated independently at each observation time t and previous time information is not required in this computational process. Moreover, the time-step size Δt of FILT can be selected as an arbitrary number and our method is suitable for the parallel computing. Later, we will discuss load distribution techniques for efficient computation.

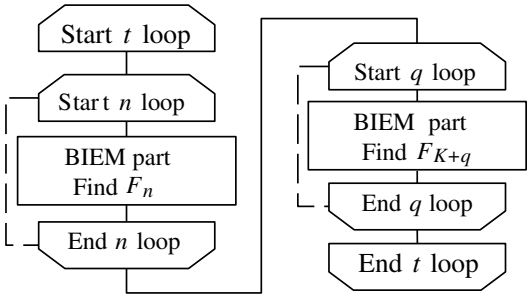

Figure 2. Flowchart for time domain analysis. The former loop is main loop for FILT. The latter loop indicates the Euler transformation to achieve rapid convergence.

3. COMPUTATIONAL RESULTS

3.1. Computational Reliability

To validate the computational accuracy of our method, we investigate eigenmodes for a metallic nanosphere shown in Table 1. The exact value for each mode number can be obtained by the exact Mie theory. When the number of unknowns N is larger than 1,000, the relative error defined by the difference between the exact and computational result is less than 1%.

Table 1. Comparison of computational eigenvalues and exact solutions for a nanosphere.

Mode number	Eigenvalues	
	Exact solution	Computed values
1	3	3.00564
2	3	3.00580
3	3	3.00584
4	5	5.01778
5	5	5.01919
6	5	5.01936
7	5	5.01976
8	5	5.02002

The time domain response of the electric field for a gold nanosphere is studied. The incident wave is a rectangular laser pulse such as

$$f_{in}(t) = \begin{cases} 0 & t < 0 \\ \sin \omega_k t & 0 \le t \le 150\,\text{fs} \\ 0 & 150\,\text{fs} < t \end{cases}, \tag{25}$$

where ω_k is the angular frequency for the mode k and is determined by the eigenmode analysis. Figure 3(a) shows the time domain response of the electric field. Here, the amplitude of the electric field is normalized by the maximum value. The electric field increases as time advances and it decreases after $t > 150\,\text{fs}$. The comparison between the computational result and exact solution [9] is shown in Figure 3(b). Both results are in excellent agreement.

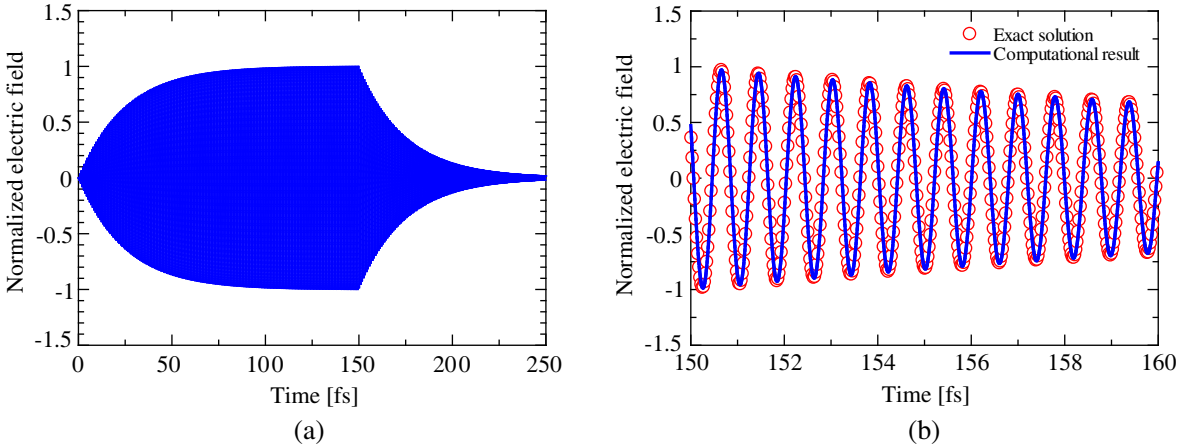

Figure 3. Time response for a specific resonance mode of a nanosphere. (a) Time domain response of electric field from 0 to 250 fs. (b) Comparison between the computational result and the exact solution.

In order to reduce the computational time for estimating the transient states, we achieve fast computation to select a relatively large time-step size. Figure 4(a) shows the time response for a gold nanosphere when a sinusoidal wave with the angular frequency ω impinges. Compared to the conventional the FDTD method for selecting the cell size $\Delta x = \Delta y = \Delta z = 1.0\,\text{nm}$, our time-step size is over 200 times as large. The relative error between the computational result and exact solution for each observation time is plotted in Figure 4(b). The error can be controlled to be less than 1% at all the sampling points.

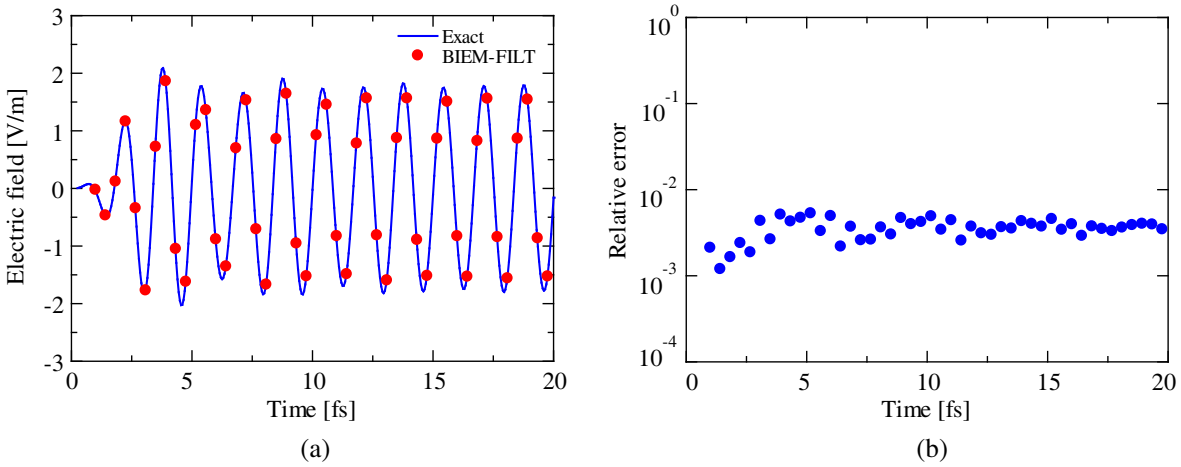

Figure 4. Time domain analysis using a large time-step size. (a) Time domain response of electric field. (b) Relative error for each sampling point.

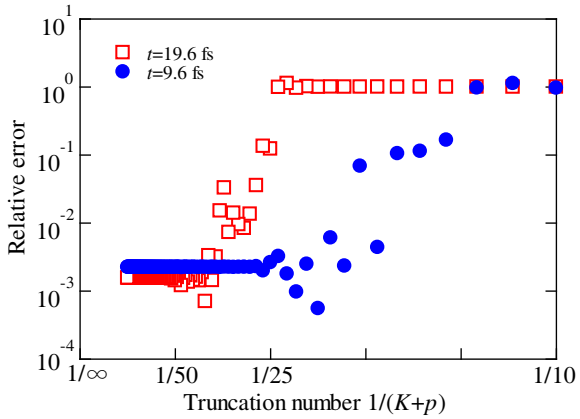

Figure 5. Convergence process of the relative error for variations in the truncation number. Circle and square dots indicate relative error of 9.6 fs and that of 19.6 fs, respectively.

Next, the error control method of the time domain analysis is discussed in detail. The convergence process of the relative error for variations in the truncation number in Eq. (23) is shown in Figure 5. We choose the Euler transformation number $p = 2$ and the approximation $\alpha = 3$. Although the truncation number increases for the later sampling point $t = 19.6$ fs, the error converges to the same approximate value 10^{-3}.

The computational time is examined using a parallel computing system. Here, we discuss two types of load distribution techniques. Figures 6(a) and 6(b) show examples of time domain responses for Cases 1 and 2, respectively. In Case 1, the entire time domain is divided into the number of blocks which have the same period. Tasks are distributed to each computer as the unit of the block. In Case 2, we distribute tasks to each computer, one by one in chronological order. Results computed by both techniques are in complete agreement.

The computational time and speed up rate of the two techniques are shown in Figures 7(a) and 7(b), respectively. The speed up rate is defined by the ratio of computational time for multiple computers to that for one computer. The computational time can be reduced by using multiple computers. When the number of computers is 10, the speed up rates are 5.61 for Case 1 and 9.88 for Case 2, respectively.

To verify that Case 2 is more effective, the computational time for variations in the sampling point is examined in Figure 7(c). The computational time is almost proportional to the observation time indicated by the horizontal axis and varies in a staircase pattern, since the truncation number K for

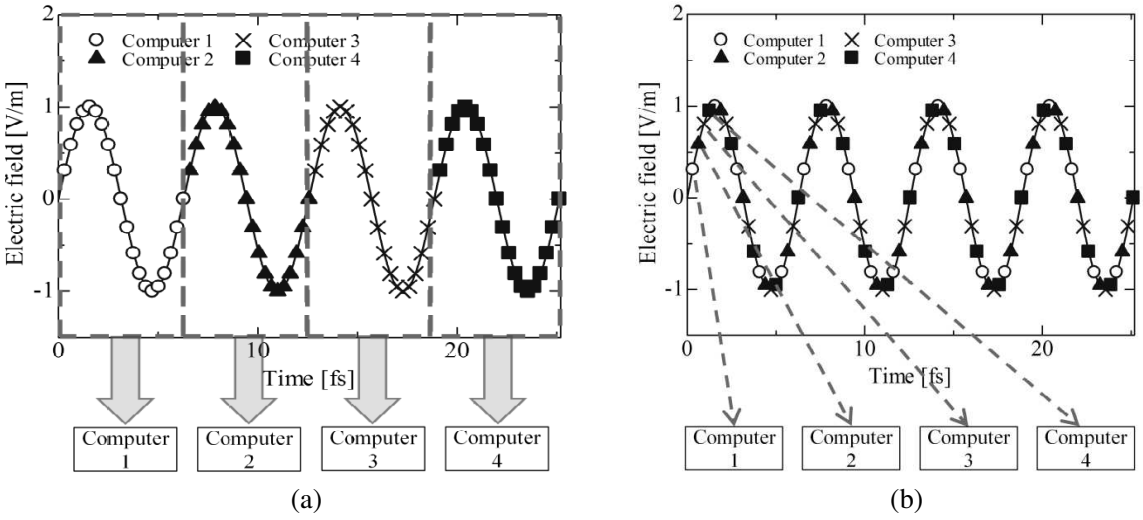

Figure 6. Load distribution techniques for parallel computing. (a) The entire time domain is divided into the number of blocks. (b) Tasks are distributed to each computer, one by one in chronological order.

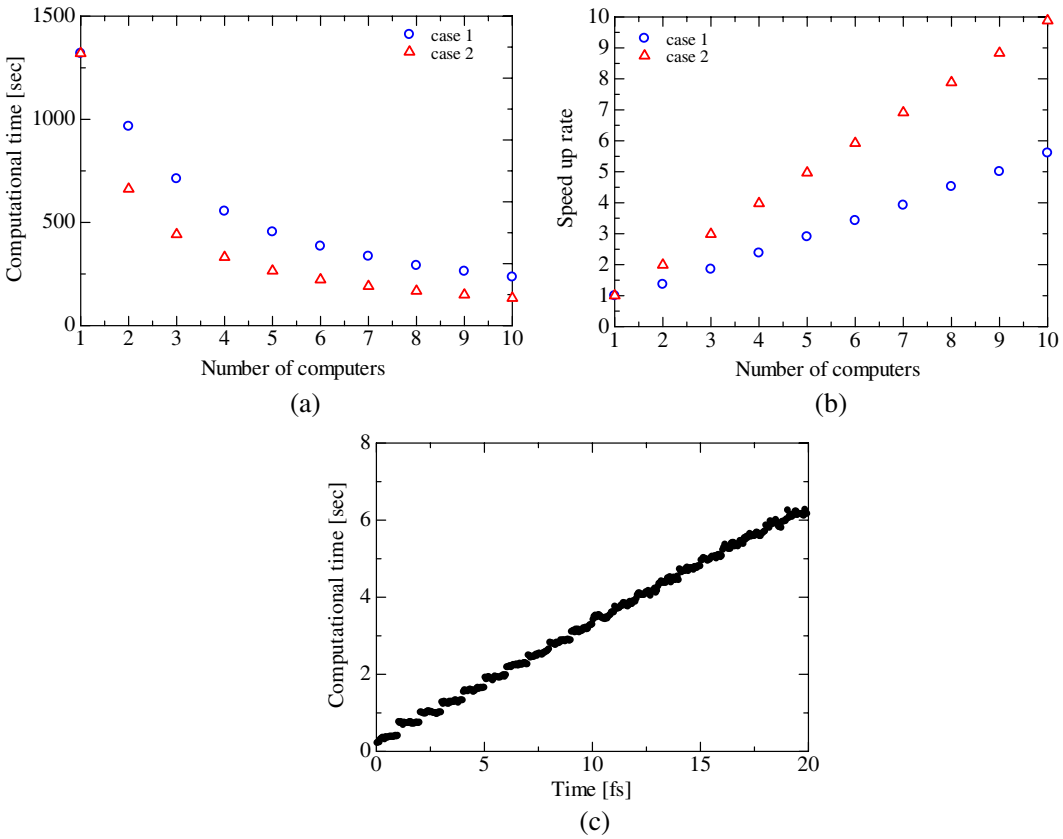

Figure 7. Computational time and speed up rate using parallel computing systems. (a) Computational time. (b) Speed up rate. (c) Computational time for each sampling point.

the observation time t is selected using $K = (\mathrm{int}(t \times 10^{15}) + 1) \times 3$. This formula is obtained by the linear interpolation selecting two sufficient truncation numbers in Figure 4. Due to this property of BIEM-FILT, Case 2 in chronological order is more effective for reducing the computational time, and the parallel efficiency is close to 100%.

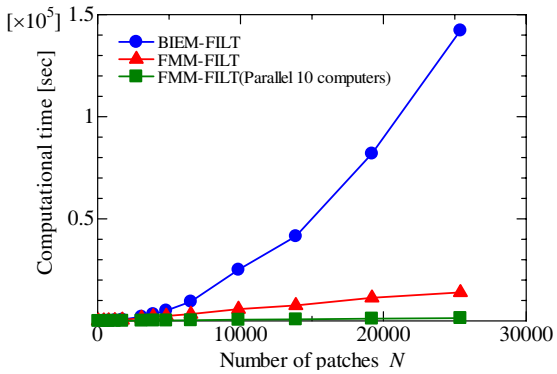

Figure 8. The computational time for varing the number of unknowns by FMM with parallel computing. Circle dots, triangulr dots, and square dots indicate ordinary BIEM-FILT, FMM-FILT, and FMM-FILT with parallel computing, respectively.

Figure 8 shows the computational time for variations in the number of unknowns. Here, we apply the fast multipole method (FMM) to BIEM part. The load distribution technique is selected as Case 2. When the number of unknowns is about 25,000, FMM with parallel computing is over 100 times faster than ordinary BIEM-FILT.

3.2. Design of Nanoscale Antennas

We design nanoscale antennas for ultra-fast and high-density magnetic recording as shown in Figure 9. The resonant wavelength of the nanoscale antenna is investigated by eigenmode analysis. Table 2 shows the eigenvalue, resonant wavelength, and dipole moment for each plasmonic resonance mode. The dipole moment is computed by

$$\mathbf{P}_k = \int_{\Omega} \mathbf{r}\sigma_k(r)d\Omega. \tag{26}$$

The dimension of the nanoscale antenna is normalized by the maximum length from the antenna center. Figure 10 shows the surface charge distribution for each mode. The incident wave has x and y components of the electric field and is assumed to be circularly polarized. We investigate resonance modes for which the electric field at the antenna center can be enhanced. The x and y components of the electric field become higher for modes 2, 3, 5, and 6, considering the x and y components of dipole moments. The wavelength response of the electric field is shown in Figure 11. The observation point is

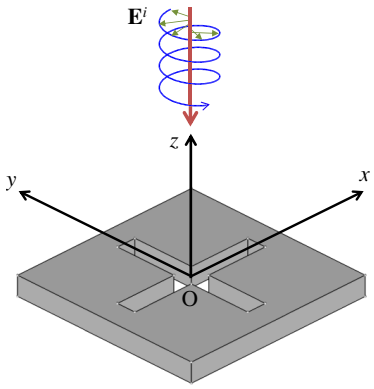

Figure 9. Geometry of a nanoscale antenna which is cross aperture type antenna. The incident wave is assumed to be the circularly polarization.

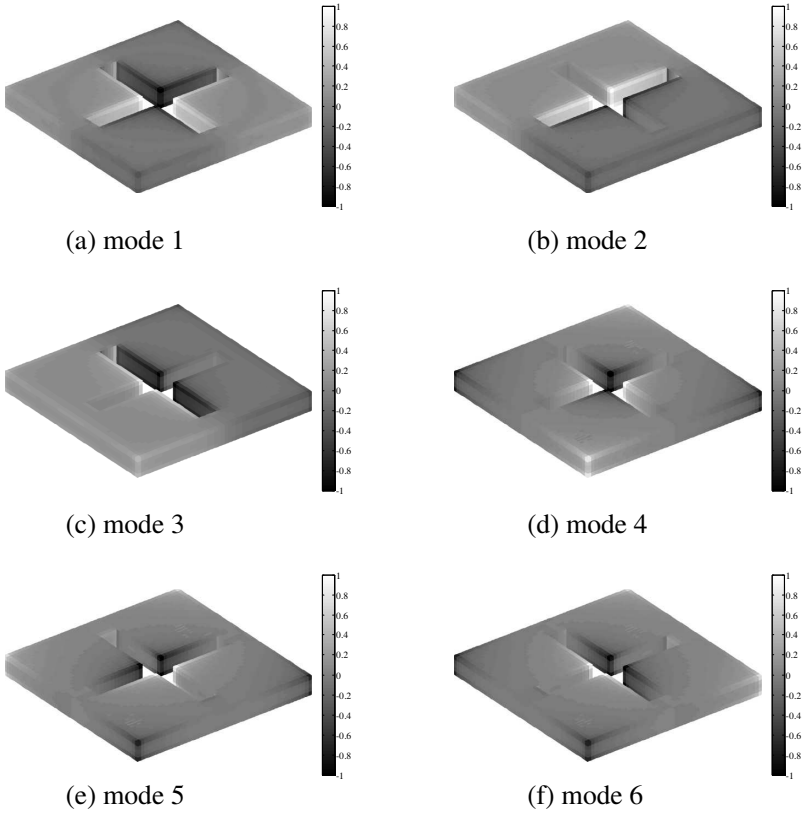

Figure 10. Surface charge distribution for each mode. White and black indicate plus charge and minus charge distribution, respectively.

Table 2. Eigenvalues, resonant wavelength, and dipole moments for each mode.

Mode number	Eigenvalues	Wavelength [nm]	Dipole moments $\mathbf{P}_k$ [C m]		
			P_{kx}	P_{ky}	P_{kz}
1	1.0674	873.1	1.5066e-15	3.0692e-15	−4.0048e-17
2	1.0475	1020.4	−3.3044e-9	0.24406	2.1955e-18
3	1.0475	1020.4	−0.24407	−1.0834e-10	2.1938e-18
4	1.2363	538.2	−2.1443e-16	1.1334e-14	−1.6946e-18
5	1.2633	520.3	−8.0464e-11	0.10458	−1.1302e-18
6	1.2633	520.3	0.10458	4.1342e-11	8.6626e-18

the antenna center. When the wavelength corresponds to the one obtained by the eigenmode analysis, the intensity becomes higher.

The transient state of the electric field for the nanoscale antenna needs to be investigated for estimating the recording process. The time domain response of the electric field evaluated at the antenna center is illustrated in Figure 12. To reduce the computational time, four sampling points are selected in one period and parallel computing is performed. We easily estimate the time to reach the steady state using this coarse time-step. In this example, the response becomes stable after 50 fs. If the response varies rapidly, we can select denser sampling points to investigate the transient process in detail. The computational results from 10 to 20 fs with the higher sampling rate are indicated by the cross dots. Compared with the computational results obtained by the FDTD method, all the results are in excellent agreements.

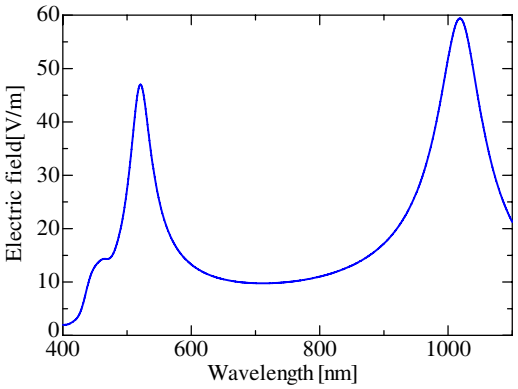

Figure 11. Wavelength response of the electric field at the antenna center. Resonances can be observed around wavelength obtained by eigenmode analysis.

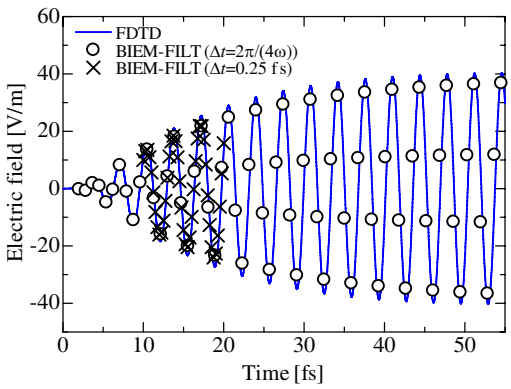

Figure 12. Time domain response of electric field for the nanoscale antenna. Circle dots and cross dot indicate computational results obtained by BIEM-FILT. The solid line indicates computational results obtained by the FDTD method.

4. CONCLUSIONS

In this paper, electromagnetic problems for nanoscale antennas have been designed by a boundary integral equation in the complex frequency domain with fast inverse Laplace transform. Our proposed method is highly efficient, and analysis of nanoscale antennas has been performed in terms of the resonant wavelength and transient state of electric fields. To obtain high intensity localized light, the resonant wavelength was computed by eignemode. We have verified that there is no computational restriction for selecting time-step size and that reliable simulation can be performed. The parallel computing and load distribution techniques are also discussed. We confirm that the computational time can be greatly reduced using a parallel computing system, and the efficiency is close to 100% .

ACKNOWLEDGMENT

This work was partly supported by JSPS KAKENHI Grant Number 26420321 and a MEXT-Supported Program for the Strategic Research Foundation at Private Universities, 2013–2017.

REFERENCES

1. Nakagawa, K., J. Kim, and A. Itoh, "Near-field optically assisted hybrid head for self-aligned plasmon spot with magnetic field," *Journal of Applied Physics*, Vol. 99, No. 8, 08F902-1–08F902-3, 2006.
2. Ota, T., Y. Ashizawa, K. Nakagawa, S. Ohnuki, H. Iwamatsu, A. Tsukamoto, and A. Itoh, "Dependence of circularly polarized light excited by plasmon aperture on relative position to magnetic particles for all-optical magnetic recording," *J. Magn. Soc. Jpn.*, Vol. 36, 66–69, 2012.
3. Kishimoto, S., T. Okada, Y. Kitaoka, S. Ohnuki, Y. Ashizawa, and K. Nakagawa, "Transient analysis of near-field light from metallic nanoparticles by BIEM-FILT," *Proceedings of IEEE AP-S/URSI 2010*, 1104–1105, Spokane, Washington, USA, Jul. 2010.
4. Kishimoto, S., S. Ohnuki, Y. Ashizawa, K. Nakagawa, and W. C. Chew, "Time domain analysis of nanoscale electromagnetic problems by a boundary integral equation method with fast inverse laplace transform," *Journal of Electromagnetic Waves and Applications*, Vol. 26, Nos. 8–9, 997–1006, 2012.

5. Nakagawa, K., Y. Ashizawa, S. Ohnuki, A. Itoh, and A. Tsukamoto, "Confined circularly polarized light generated by nano-size aperture for high density all-optical magnetic recording," *Journal of Applied Physics*, Vol. 109, 07B735-1–07B735-3, 2011.
6. Biagioni, P., J. S. Huang, L. Duo, M. Finazzi, and B. Hecht, "Cross resonant optical antenna," *Physical Review Letters*, Vol. 102, 256801-1–256801-4, 2009.
7. Biagioni, P., M. Savoini, J.-S. Huang, L. Duo, M. Finazzi, and B. Hecht, "Near-field polarization shaping by a near-resonant plasmonic cross antenna," *Physical Review B*, Vol. 80, 153409-1–153409-4, 2009.
8. Stanciu, C. D., F. Hansteen, A. V. Kimel, A. Kirilyuk, A. Tsukamoto, A. Itoh, and T. Rasing, "All-optical magnetic recording with circularly polarized light," *Physical Review Letters*, Vol. 99, 047601-1–047601-4, 2007.
9. Mayergoyz, I. D., Z. Zhang, and G. Miano, "Analysis of dynamics of excitation and dephasing of plasmon resonance modes in nanoparticles," *Physical Review Letters*. Vol. 98, No. 14, 147401-1–147401-4, 2007.
10. Fredkin, D. R. and I. D. Mayergoyz, "Resonant behavior of dielectric objects (electrostatic resonance)," *Physical Review Letters*, Vol. 91, 253902-1–253902-4, 2003.
11. Mayergoyz, I. D., D. R. Fredkin, and Z. Zhang, "Electrostatic (plasmon) resonance in nanoparticles," *Physical Review B*, Vol. 72, 155412-1–155412-15, Condens. Matter, 2005.
12. Rakić, A. D., A. B. Djurišić, J. M. Elazar, and M. L. Majewski, "Optical properties of metallic films for vertical-cavity optoelectronic devices," *Applied Optics*, Vol. 37, No. 22, 5271–5283, 1998.
13. Hosono, T., "Numerical inversion of laplace transform and some applications to wave optics," *Radio Science*, Vol. 16, 1015–1019, 1981.